

Structural Origin of Reversible Li Insertion in Guest-Free, Type-II Silicon Clathrates

Andrew Dopilka, J. Mark Weller, Alexander Ovchinnikov, Amanda Childs, Svilen Bobev, Xihong Peng, and Candace K. Chan*

The guest-free, type-II Si clathrate (Si_{136}) is an open cage polymorph of Si with structural features amenable to electrochemical Li storage. However, the detailed mechanism for reversible Li insertion and migration within the vacant cages of Si_{136} is not established. Herein, X-ray characterization and density functional theory (DFT) calculations are used to understand the structural origin of electrochemical Li insertion into the type-II clathrate structure. At low Li content, instead of alloying with Si, topotactic Li insertion into the empty cages occurs at ≈ 0.3 V versus Li/Li^+ with a capacity of $\approx 231 \text{ mAh g}^{-1}$ (corresponding to composition $\text{Li}_{32}\text{Si}_{136}$). A synchrotron powder X-ray diffraction analysis of electrodes after lithiation shows evidence of Li occupation within the Si_{20} and Si_{28} cages and a volume expansion of 0.22%, which is corroborated by DFT calculations. Nudged elastic band calculations suggest a low barrier (0.2 eV) for Li migration through interconnected Si_{28} cages, whereas there is a higher barrier for Li migration into Si_{20} cages (2.0 eV). However, if Li is present in a neighboring cage, a cooperative migration pathway with a barrier of 0.65 eV is possible. The results show that the type-II Si clathrate displays unique electrochemical properties for potential applications as Li-ion battery anodes.

as promising candidates for thermoelectric materials,^[1] clathrates also have interesting properties for optoelectronics^[2–4] and superconducting^[5–7] applications. Due to the large interest in Tt elements as high-capacity Li-ion battery anodes, the electrochemical properties of Tt clathrates have also been investigated in recent years, revealing properties distinct from those of diamond cubic structured analogues.^[8–18] For instance, the reaction of Li with the type-I clathrate $\text{Ba}_8\text{Al}_6\text{Si}_{30}$ is dominated by surface rather than bulk reactions,^[15] whereas the $\text{Ba}_8\text{Al}_y\text{Ge}_{46-y}$ ($0 < y < 16$) clathrate undergoes bulk phase transitions to form amorphous Li–Ba–Ge phases with local structures similar to those in Li–Ge crystalline phases.^[10,16] For the type-II clathrate $\text{Na}_{24}\text{Si}_{136}$, the lithiation profile is similar to that for diamond cubic Si,^[12] whereas $\text{Na}_{1.6}\text{Si}_{136}$ displays one more similar to that of amorphous Si.^[8] Due to the wide range of possible clathrate structures and compositions,^[1] we are interested in

establishing a better understanding of the structure–property relationships of clathrates within the context of Li-ion battery applications.

Clathrates crystallize in a variety of structural types where different face-sharing polyhedra are built from tetrahedral bonding

1. Introduction

Tetrel (Tt = Si, Ge, Sn) clathrates are host–guest materials comprising cage frameworks of Tt elements that encapsulate alkali metal and alkaline earth metal guest atoms. Well known


A. Dopilka, J. M. Weller, Prof. C. K. Chan
Materials Science and Engineering
School for Engineering of Matter, Transport and Energy
Arizona State University
P.O. Box 876106, Tempe, AZ 85827, USA
E-mail: candace.chan@asu.edu

Dr. A. Ovchinnikov, A. Childs, Prof. S. Bobev
Department of Chemistry and Biochemistry
University of Delaware
Newark, DE 19716, USA

Dr. A. Ovchinnikov
Department of Materials and Environmental Chemistry
Stockholm University
Svante Arrhenius väg 16 C, Stockholm 10691, Sweden

Prof. X. Peng
College of Integrative Sciences and Arts
Arizona State University Polytechnic Campus
Mesa, AZ 85212, USA

Prof. C. K. Chan
Department of Heterogeneous Catalysis
Max-Planck-Institut für Kohlenforschung
Kaiser-Wilhelm-Platz 1, Mülheim an der Ruhr 45470, Germany

 The ORCID identification number(s) for the author(s) of this article can be found under <https://doi.org/10.1002/aesr.202000114>.

© 2021 The Authors. Advanced Energy and Sustainability Research published by Wiley-VCH GmbH. This is an open access article under the terms of the Creative Commons Attribution License, which permits use, distribution and reproduction in any medium, provided the original work is properly cited.

DOI: 10.1002/aesr.202000114

of Tetrrel elements. The type-II clathrate is described by the $Fd\bar{3}m$ space group and has a general formula of $M_{24}Tt_{136}$, where M are alkali or alkaline earth metals (e.g., Na, K, Cs, Ba).^[19] In a single unit cell, the structure is composed of eight Tt_{28} cages (hexakaidecahedra) and 16 Tt_{20} cages (dodecahedra). The Tt atoms reside at the vertices of the polyhedra and form hexagonal or pentagonal faces, whereas the guest atoms occupy the center positions. **Figure 1a** shows a model of a Si_{20} cage (yellow) and Si_{28} (black) cage occupied by Na guest atoms from the structure of a Na-filled type-II silicon clathrate. In this structure, the Si_{28} cages, composed of four hexagons and 12 pentagons, form a face-sharing tetrahedral network connected by the four hexagonal faces (**Figure 1b**). The Si_{20} cages, composed of 12 pentagons, fill the space between the Si_{28} cages by forming perpendicular channels, which can be seen in the [011] direction (**Figure 1c**). **Figure 1d** shows a larger polyhedral model to illustrate the connectivity between the two types of cages. Deviation from the general formula of $M_{24}Tt_{136}$ is often observed in clathrates with guest atom vacancies ($M_{24-x}Tt_{136}$)^[19–21] and framework substitutions ($M_{24}A_xTt_{136-x}$, A = another element substituting Tt).^[22–24] These defects or combination of defects result in a wide structural landscape for controlling the materials properties of Tt clathrates.

The type-II clathrate $Na_{24-x}Si_{136}$ ^[19,25,26] is notable for having a tunable Na content. For Li-ion battery applications, the removal of Na from the cages provides the opportunity for using the guest-free clathrates as Li-ion battery electrodes. Langer et al. used nuclear magnetic resonance (NMR) spectroscopy to demonstrate that electrochemical insertion of Li into $Na_{1.6}Si_{136}$ takes place at 0.3 V versus Li/Li⁺.^[8] However, the reversibility of this

insertion process was not evaluated, and the Li positions and migration pathways within the cages were not resolved.

Herein, we undertake a detailed investigation to establish the structural origin and mechanism for Li insertion into type-II Si_{136} clathrates with low Na content. Using electrochemical analysis, synchrotron X-ray diffraction (XRD), and density functional theory (DFT) calculations, a reversible topotactic Li insertion process is identified in nearly guest-free clathrate $Na_{0.9}Si_{136}$, which is accompanied by a volume expansion of 0.22% after Li occupation of both Si_{20} and Si_{28} cages. The Li positions in the larger Si_{28} cages are significantly off-center, pointing to the possibility of high disorder and the presence of multiple Li atoms inside the Si_{28} cages. DFT calculations show that the Li positions predicted to be most favorable match closely with those found from XRD refinement. Nudged elastic band (NEB) calculations are used to investigate the Li migration pathways and show that Li migration should be dominant through the interconnected network of Si_{28} cages due to the low migration barrier of 0.20 eV. Li migration into Si_{20} cages is predicted to be kinetically limited unless there is a neighboring Li atom, which enables an alternative bond-breaking pathway with a lower energy barrier of 0.65 eV. Overall, the results show how Li insertion into the vacant cages of the type-II Si clathrate structure can be promising for Li-ion anodes due to the low reaction voltage (0.3 V vs Li/Li⁺) and negligible volume expansion (0.22%) coupled with a suitable capacity ($\approx 230 \text{ mAh g}^{-1}$). We identify Li migration through the hexagonal faces between interconnected cages as an important condition for bulk Li diffusion. Based on this structural feature, other open Tetrrel frameworks are identified that could have analogous Li insertion/deinsertion behavior.

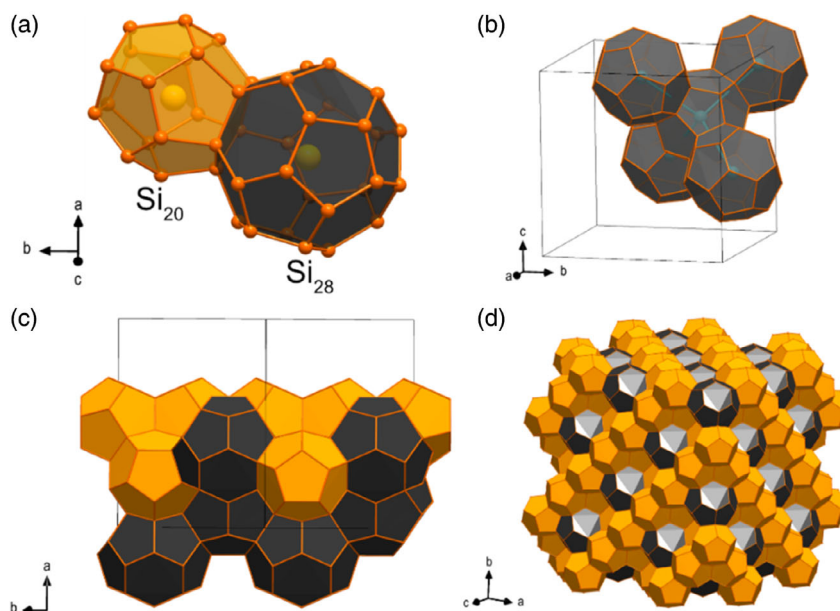


Figure 1. a) Crystal model showing the two types of polyhedra in the type-II clathrate $Na_{24-x}Si_{136}$ ($0 < x < 24$) structure: the dodecahedra (Si_{20}) in yellow and the hexakaidecahedra (Si_{28}) in black. b) Polyhedral model showing the network of Si_{28} cages connected by shared hexagonal faces. The blue spheres and bonds indicate the tetrahedral arrangement of the connected Si_{28} cages. Polyhedral view of the type-II clathrate structure c) viewed down the [011] direction and d) $2 \times 2 \times 2$ supercell showing both Si_{20} and Si_{28} cages.

2. Results and Discussion

2.1. Structural Characterization of As-Synthesized $\text{Na}_{24-x}\text{Si}_{136}$ Samples

To understand the role of guest atom occupancy on the electrochemical reaction of Li with type-II Si clathrates, two samples with different Na contents were prepared (see Figure S1, Supporting Information) and then characterized with synchrotron powder XRD (PXRD). The first sample was heated under vacuum for 5 days to lower the Na content to near guest-free concentrations. The PXRD pattern of this sample confirms that the sample contains predominately the type-II clathrate phase with small impurities from the type-I clathrate phase (Figure 2a). The Rietveld refinement (Table S1, Supporting Information) of this sample resulted in a composition of $\text{Na}_{0.9(1)}\text{Si}_{136}$ with a lattice parameter of 14.6460(1) Å, so this sample will be referred to as “Na1” from now on. The second sample was heated under

vacuum for 30 h to target a type-II Si clathrate sample with intermediate Na content. The Rietveld refinement (Figure 2b, and Table S2, Supporting Information) of this sample resulted in a composition of $\text{Na}_{10.7(1)}\text{Si}_{136}$ (hence, we refer to this as the “Na11” sample) with a lattice parameter of 14.6544(2) Å and 1.4 wt% impurity of $\text{Na}_8\text{Si}_{46}$. The lattice constants, atomic coordinates, and displacement parameters match well with previous PXRD and single crystal XRD refinements of type-II Si clathrates with different Na contents.^[27,28] For Na11, the large Si_{28} cages were found to be preferentially occupied by Na over the Si_{20} cages, consistent with previous XRD analyses.^[8,26–28]

Scanning electron microscopy (SEM) imaging showed that the clathrate particles were comprised of particles (3–11 μm) decorated with smaller protrusions (Figure S2a,b, Supporting Information). Transmission electron microscopy (TEM) showed that the clathrate particles are polycrystalline, with the selected area electron diffraction (SAED) pattern showing reflections corresponding to different orientations of crystalline domains

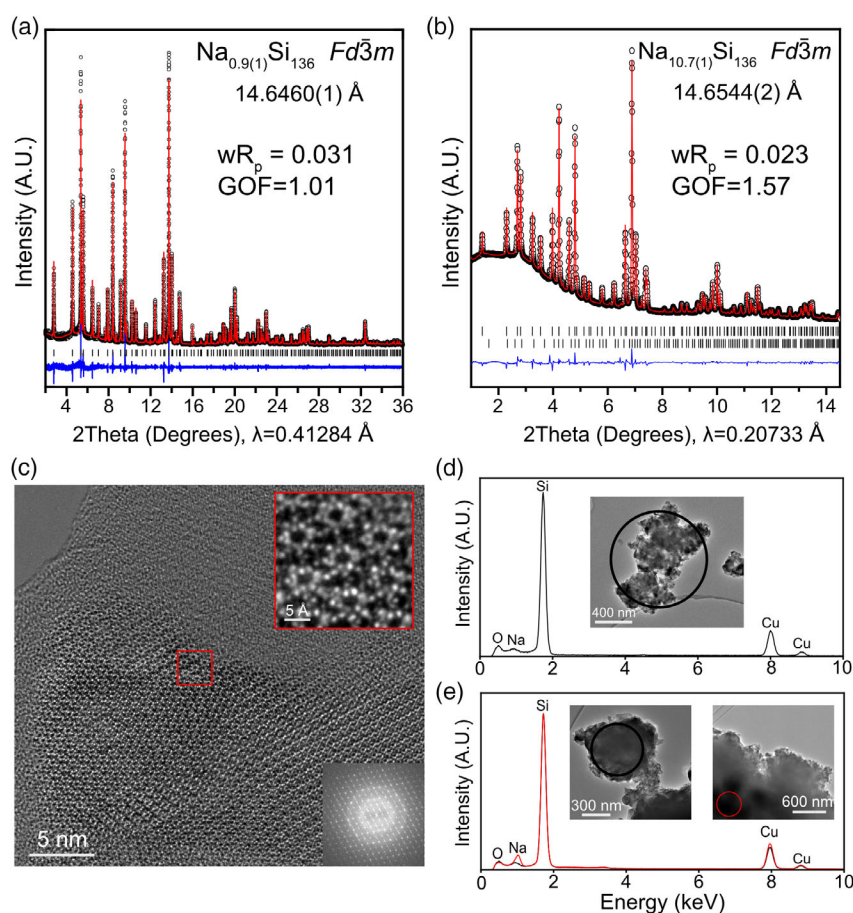


Figure 2. Rietveld refinement of the PXRD patterns of the a) Na1 and b) Na11 samples. The black circles represent the experimental pattern, the red curve represents the calculated pattern, and the blue curve represents the difference curve. Tick marks indicate the reflection positions. In (b), the top set of marks correspond to the type-II phase, whereas the bottom ticks correspond to the type-I clathrate phase. The refined atomic positions, occupancies, and atomic displacement parameters can be found in Table S1-2, Supporting Information. c) HRTEM image of Na1 along the [110] zone axis with inset showing the characteristic cage structure of the type-II Si clathrate of the region indicated with the red box. Bottom right inset is a fast Fourier transform (FFT) of the image showing the spot pattern of the [110] zone axis. d) TEM-EDS data from Na1 (taken from area indicated by black circle) and e) two areas in the Na11 sample (the red curve is the EDS spectrum from the middle of a thicker part of the particle as indicated by the red circle). The Cu signal is from the copper TEM grid.

(Figure S2c, Supporting Information) and high-resolution TEM (HRTEM) imaging revealing the type-II cage structure (Figure 2c). Energy dispersive X-ray spectroscopy (EDS) conducted in the TEM detected signals from O, Na, Si, and Cu (from the TEM grid) for both Na1 and Na11 samples (Figure 2d,e), consistent with the presumed composition of the samples based on the XRD patterns. For Na11, the Na composition varied depending on the area of interest (Figure 2e). When an EDS spectrum was collected from a small particle, the Na content was similar to that of the Na1 sample. When the EDS spectrum was collected from a thicker area near the center of a larger particle, the Na content was higher than in the Na1 sample, which is consistent with the higher average Na content of Na11. This variation of the Na content based on the particle size is likely due to Na evaporation during the synthesis under vacuum, where smaller particles are expected to lose Na more quickly because of the higher surface area and shorter diffusion lengths.

2.2. Electrochemical Li Insertion into Si_{136}

Voltage profiles corresponding to the first full lithiation of Na1 and Na11 type-II Si clathrates are shown in Figure 3. The voltage profile for Na1 displayed plateaus at 0.30, 0.25, 0.10, and 0.05 V versus Li/Li^+ , which are more clearly discerned as peaks in the dQ/dE plot (Figure 3, inset). The plateau at 0.30 V was attributed to the insertion of Li into the cage structure by Langer et al. through NMR analysis, whereas amorphization of the Si framework was determined to begin at 0.25 V from XRD analysis.^[8] The process at 0.05 V is attributed to transformation of the amorphous Li_xSi alloy to crystalline $\text{Li}_{15}\text{Si}_4$.^[29–31] The broad peak at 0.10 V is typically not observed during lithiation of diamond Si, but rather during lithiation of amorphous Si,^[30–32] suggesting that a similar phase transformation could be occurring in the type-II clathrate at this voltage. The lithiation capacity (3700 mAh g^{-1}) for Na1 is comparable to that seen in diamond

or amorphous Si electrodes and corresponds to a Li–Si ratio close to the composition expected for the formation of $\text{Li}_{15}\text{Si}_4$ (3586 mAh g^{-1}).

The voltage profile for Na11 is distinctly different from that for Na1 and is dominated by a sloping curve (seen as a broad peak centered at 0.15 V in the dQ/dE plot). The plateau at 0.30 V attributed to Li insertion into the clathrate framework is not present in the voltage profile of Na11, suggesting that this lithiation process observed in Na1 does not occur in Na11. The small peak at 0.23 V is similar in voltage to the peak at 0.25 V in the Na1 sample, which we attribute to the presence of clathrate with low Na content as an impurity phase in the Na11 sample. This hypothesis is supported by the observed variation in Na content in small versus large particles by EDS (Figure 2e), where a small particle of Na11 was found to have a similar Na content to that of the Na1 sample. The broad peak at 0.15 V in the dQ/dE plot, attributed to the beginning of an amorphization reaction, is found at a lower voltage than the amorphization of Na1 (0.25 V) but is similar to the voltage for the amorphization of $\text{Na}_{24}\text{Si}_{136}$ (0.12 V).^[12] It is interesting to note that the amorphization potential for Na1 is around 0.15 V higher than that for diamond cubic Si, which reacts at 0.10 V,^[33] indicating that there is a significant thermodynamic or kinetic difference in the Li–Si amorphous phase conversion.

To assess the number of Li inserted into the clathrate cage structure, the capacity was measured from 0.32 to 0.26 V to remove possible contributions from formation of solid electrolyte interphase (SEI) or reactions with the carbon black additive in the electrode, as well as to avoid charge associated with the amorphization reactions. This voltage range is indicated by the blue dashed lines in the normalized dQ/dE plot in the inset of Figure 3. The resulting capacity of 236 mAh g^{-1} corresponds to a composition of $\text{Li}_{33}\text{Si}_{136}$ when attributing all of the charge transferred in this voltage region to Li insertion into the clathrate cages. This amount of capacity is notable, because it results in a larger number of guest atoms than expected for the typical type-II clathrate stoichiometry of $\text{M}_{24}\text{Tt}_{136}$, which assumes that one guest atom occupies each of the 24 cages in the unit cell. This suggests that either multiple Li are occupying the cages of the clathrate structure (which has been suggested before for $\text{Li}_x\text{Ge}_{136}$ ^[11]), or there is another reaction mechanism occurring that is contributing to the capacity. Previously, the synthesis of $\text{Na}_{30.5}\text{Si}_{136}$ was demonstrated where two Na atoms were shown to occupy a single Si_{28} cage.^[34] Considering the smaller size of Li atoms, we speculate that multiple Li atoms occupying a single Si_{28} cage could also be possible. To further investigate this possibility, synchrotron PXRD measurements were performed for lithiated type-II clathrate samples.

2.3. Synchrotron X-ray Powder Diffraction of Lithiated Si_{136}

To obtain insight into the Li positions in the clathrate structure, synchrotron PXRD was conducted on the Na1 sample after electrochemical lithiation. Lithiation was performed with a cutoff voltage of 0.26 V versus Li/Li^+ to prevent the start of the two-phase amorphization reaction. The voltage profile and corresponding dQ/dE plot are presented in Figure 4a, with a capacity of around 207 mAh g^{-1} (corresponding to a composition

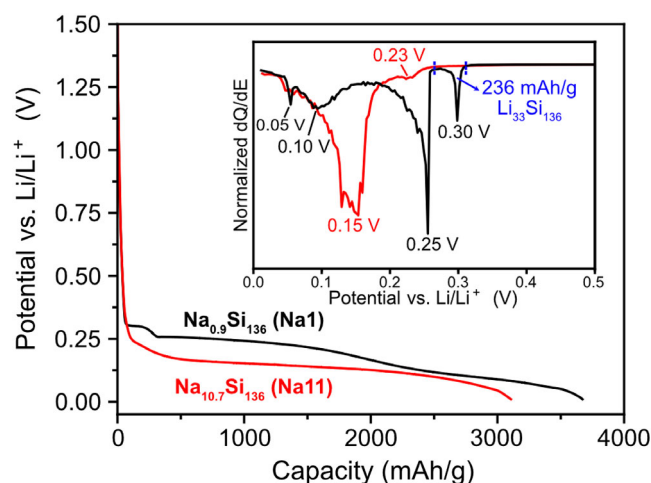


Figure 3. Voltage curve for galvanostatic lithiation of type-II clathrate with compositions of $\text{Na}_{0.9}\text{Si}_{136}$ (Na1, black trace) and $\text{Na}_{10.7}\text{Si}_{136}$ (Na11, red trace) at 25 mA g^{-1} with a 0.01 V versus Li/Li^+ cutoff. The inset is the normalized dQ/dE plot derived from the voltage profiles. The blue dashed lines indicate the voltage range attributed to Li insertion into Si_{136} .

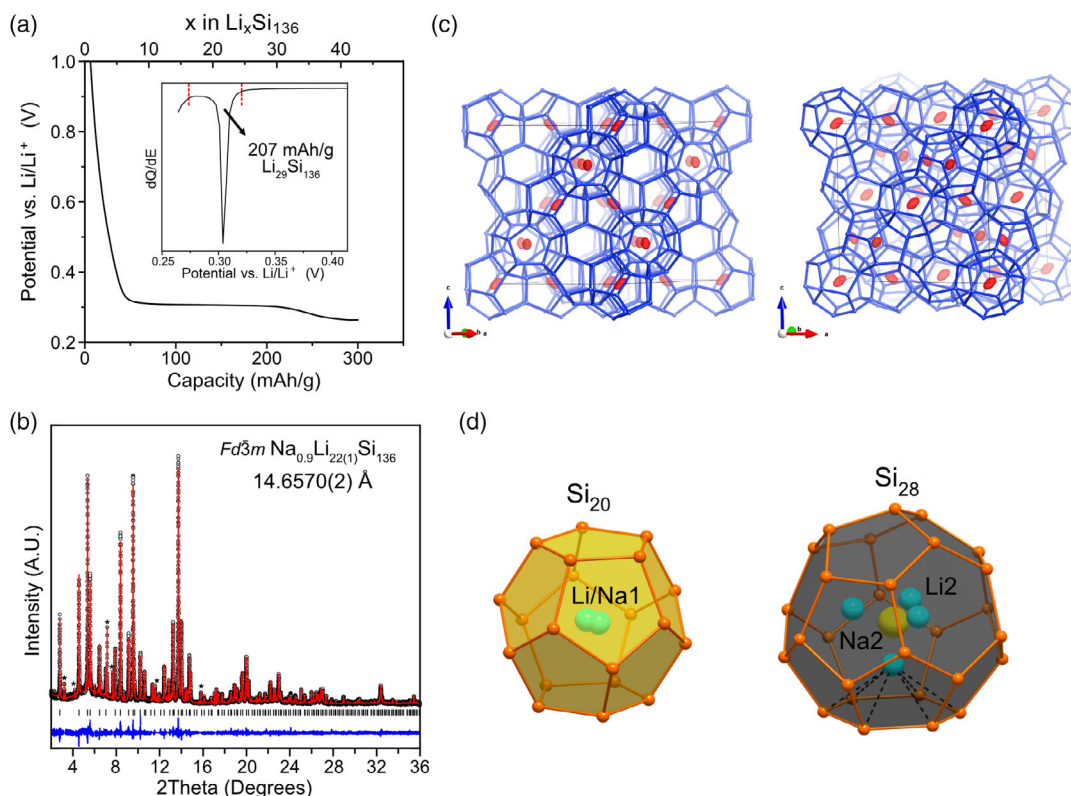


Figure 4. Analysis of Li insertion into Na₁Si₁₃₆ (Na1). a) Galvanostatic voltage profile and corresponding dQ/dE plot of a Na1 electrode lithiated at 10 mA g⁻¹. The red lines indicate the voltage range (0.27–0.32 V) in which the dQ/dE plot was integrated to determine an approximate composition of Li₂₉Si₁₃₆ after lithiation. b) Synchrotron PXRD ($\lambda = 0.412781$ Å) of the lithiated clathrate (black = observed, red = simulated, blue = difference curve, and tick marks = positions of reflections; the stars mark an unknown impurity phase present in the XRD pattern, which was omitted for the refinement. c) Residual electron density peaks (isosurface level 0.8 e Å⁻³) from the difference Fourier mapping in the small Si₂₀ cages from the pattern in (b). The blue atoms represent Si, whereas the red surfaces represent the isosurface of the residual electron density. d) Atomic positions used in the refinement for Na (yellow) and Li (cyan) guest atoms in the Si₂₀ and the Si₂₈ cages. The black dotted lines are the Li–Si bonds between the off-center Li to the Si atoms comprising the hexagonal face.

of Li₂₉Si₁₃₆) attributed to Li insertion into the clathrate cages only.

The PXRD pattern for the lithiated Na1 clathrate sample is shown in Figure 4b and was refined to a larger lattice parameter of 14.6570(2) Å compared with that in the as-synthesized, unlithiated sample (Figure 2a), corresponding to a 0.22% volume expansion. This indicates a small expansion in the Si framework after electrochemical lithiation. To analyze the possible Li positions in the clathrate, the pattern was fit to the guest-free Si₁₃₆ structural model, and then, difference Fourier mapping was used to identify residual electron density in the clathrate cages. The results show that significant electron density is shifted slightly off the center of the Si₂₀ cages (Figure 4c). When the electron density was modeled as pure Na, this position refined to an occupancy of 9%, which is much larger than the value found for this site in the pristine Na1 ($\approx 2\%$). Even without considering the Si₂₈ cages, a 9% occupation of this position by Na would result in a higher Na content than what was present in the unlithiated clathrate. This finding suggests that the electron density in the Si₂₀ cages originates from the presence of both Na and Li. To properly handle the mixed occupation and under occupation, the

occupancy of Na was set to the value refined in the unlithiated clathrate, whereas the occupancy of Li (located in the same site) was allowed to vary.

In addition, the larger Si₂₈ cages were found to accommodate well-structured residual electron density with a maximum located close to the center of the cage and four maxima shifted from the center toward the hexagonal faces in the form of a tetrahedron. A small occupation of the central position in the Si₂₈ cages was detected for the pristine Na1 clathrate as well. Furthermore, the absolute value of the residual electron density in this position for the lithiated clathrate corresponds to the same occupancy by Na as in the unlithiated Na1. Therefore, this position was treated as pure Na. The four peaks situated closer to the hexagonal faces were refined as partially occupied Li sites, based on the distances to the adjacent Si sites.

The positions of the Na and Li atoms used in the refinement are shown in Figure 4d. The Li position in the Si₂₀ cage refined to an occupation of 0.33, which corresponds to 10.88 Li within the 16 Si₂₀ cages, whereas the Li site in the Si₂₈ cage refined to an occupation of 0.34, corresponding to 10.8 Li in the eight Si₂₈ cages and suggesting the possibility of multiple Li atoms

within the larger cages. This resulted in a final composition of $\text{Na}_{0.9}\text{Li}_{22(1)}\text{Si}_{136}$. The atomic positions and occupancies from the refinement can be found in Table S3, Supporting Information. The refined composition contains less Li (22) than that expected based on the capacity from the voltage profile (29 Li). The electrochemical lithiation was repeated with another nearly Na-free clathrate sample prepared in a similar fashion, and additional PXRD experiments were conducted at a different beamline to confirm this result; Figure S3, Supporting Information, shows the electrochemical voltage profile and PXRD pattern before and after lithiation. The results are similar to those shown in Figure 4, with a small increase in lattice parameter and higher electron density attributed to Li occupation of both Si_{28} and Si_{20} cages after lithiation, confirming that the observed electrochemical reactions from 0.3 to 0.26 V versus Li/Li^+ correspond to Li insertion into the vacant cages of the type-II clathrate structure. These results are also consistent with the previous NMR spectroscopy measurements, which showed two distinct chemical shifts for Li, corresponding to different Li environments in the clathrate cages and chemical shift values that were higher than that for Li metal,^[8] similar to what is seen for Na NMR analysis of $\text{Na}_{24-x}\text{Si}_{136}$.^[35] Future neutron diffraction experiments would be insightful for more accurately characterizing the Li positions and occupancies in the clathrate structure.

2.4. DFT Calculations to Determine Li Positions in Si_{136}

Next, DFT calculations were used to form a theoretical basis for understanding the preferred Li positions in the type-II Si clathrate structure and the diffusion pathways between them. Similar to our previous study investigating Li migration in guest-free clathrates that adopt the type-I structure,^[17] several possible Li sites were considered, and the Gibbs free energy of reaction (ΔG_r)^[36] was evaluated as the metric for assessing the favorability of a Li position (see Supporting Information for more details). Figure 5a shows a portion of the type-II Si clathrate structure where a Si_{28} cage is shared via a pentagonal face to a Si_{20} cage, along with the Li positions identified as local energy minima from the DFT calculations—Positions 1 and 2 are found at the centers of the Si_{20} and Si_{28} cages, respectively, whereas Positions 3 and 4 are coordinated off the hexagonal (“Off Hex”) and pentagonal (“Off Pent”) faces, respectively, inside of the Si_{28} cages. Figure 5b shows additional views of the Li sites at Positions 3 and 4 with selected Si–Li bond lengths indicated. To provide a 3D view of these positions, a video showing the four positions can be found in Movie S1, Supporting Information.

Figure 5c shows the calculated change in the Gibbs free energy of reaction considering Li inserted into each of the four positions in the Si_{136} structure, where a negative value indicates a favorable reaction for the formation of LiSi_{136} with respect to Li metal and Si_{136} . The results show that Li occupation in the center of the smaller (Si_{20}) cage (Position 1) was favorable with a slightly negative Gibbs free energy of reaction (ΔG_r) of -36 meV. Among the possible sites within the Si_{28} cage, Li in the center of the cage (Position 2) was very unfavorable ($\Delta G_r = +0.467$ eV) compared with the other positions. From these results, it is expected that Li occupation of the Si_{28} cage would result in Li being off-center due to the relatively high energy of the centered position, whereas Li

in the Si_{20} cage would favor being closer to the center of the cages. These results are in good agreement with our previous calculations on the preferred Li positions in Tetrel (Tt) clathrate cages with the type-I structure, which is made up of Tt_{20} and Tt_{24} cages. In that study,^[17] we found that if the clathrate cage is sufficiently large (e.g., in the case of the Tt_{24} cages in type-I clathrates), then the lowest energy position for Li was to be coordinated off the hexagonal face with a Li–Tt (Tt = Si, Ge, and Sn) bond distance of 2.7–2.9 Å rather than at the cage center. The DFT calculated positions in Figure 5a are in good agreement with those determined from the PXRD refinement (Figure 4d). In both cases, Li is found near the center of the Si_{20} cages while coordinated off of the hexagonal faces in the Si_{28} cages. The refined Li–Si distances from the PXRD analysis were 2.86–2.90 Å for Li in the “Off Hex” position, which are slightly longer than those calculated using DFT (2.65–2.69 Å).

To evaluate the most favorable Li site in the clathrate lattice during electrochemical lithiation, the average lithiation voltage was calculated from the change in Gibbs reaction energy as a function of total Li content (Figure 5d) for select structures (Crystallographic information files are available; see Supporting Information). This analysis does not consider the many possible orderings of Li within $\text{Li}_x\text{Si}_{136}$, which would require a cluster expansion analysis to simulate the 0 K voltage profile.^[37,38] Rather, we seek to understand the energetic differences between Li occupation of the Si_{20} and Si_{28} cages. In Figure 5d,e, the indices next to each point identify the number of Li in the Si_{20} cage center or in the “Off Hex” position within the Si_{28} cages (corresponding to the first and second numbers, respectively, in the indices). When adding eight Li to the “Off Hex” positions in the Si_{28} cages, the Li is divided evenly between the eight Si_{28} cages, meaning that (0,8) and (0,16) correspond to one and two Li occupying a single Si_{28} cage, respectively. When comparing the calculated voltages in $\text{Li}_x\text{Si}_{136}$ for $x = 8$ and 16, it is more favorable for Li to occupy the Si_{20} cages, i.e., points (8, 0) and (16, 0), than the Si_{28} cages, i.e., points (0, 8) and (0, 16), based on the higher voltages calculated for the former case (which corresponds to a lower ΔG_r). However, after the 16 Si_{20} cages are each filled with a single Li in the center position, adding eight Li to the Si_{28} cages in the “Off Hex” position (corresponding to (16, 8) at $x = 24$) is favorable, on account of the positive voltage versus Li/Li^+ . This suggests that Li occupation of the Si_{28} cages is more favorable if the Si_{20} cages are filled with Li. Interestingly, as eight Li are subsequently added to the Si_{28} “Off Hex” positions (for $x = 40$ and 48), the voltage increases again, indicating the energetic feasibility for multiple Li to occupy a single Si_{28} cage. The composition of $\text{Li}_{48}\text{Si}_{136}$ corresponds to a single Li occupying the centers of each of the 16 Si_{20} cages and four Li occupying each of the eight Si_{28} cages in the “Off Hex” positions. Even without Li occupation of the Si_{20} cages, $\text{Li}_{32}\text{Si}_{136}$ (corresponding to the point (0, 32)) has a positive voltage of 0.22 V, further suggesting that multiple Li occupation of the Si_{28} cage is more favorable than occupation by a single Li atom. In short, the theoretical voltage calculations indicate an energetic preference for Li to occupy the Si_{20} cages over the Si_{28} cages and also suggest that it is energetically favorable for multiple Li to occupy a single Si_{28} cage.

The calculated lattice constants of the crystal structures for the black curve in Figure 5d are presented in Figure 5e. For the

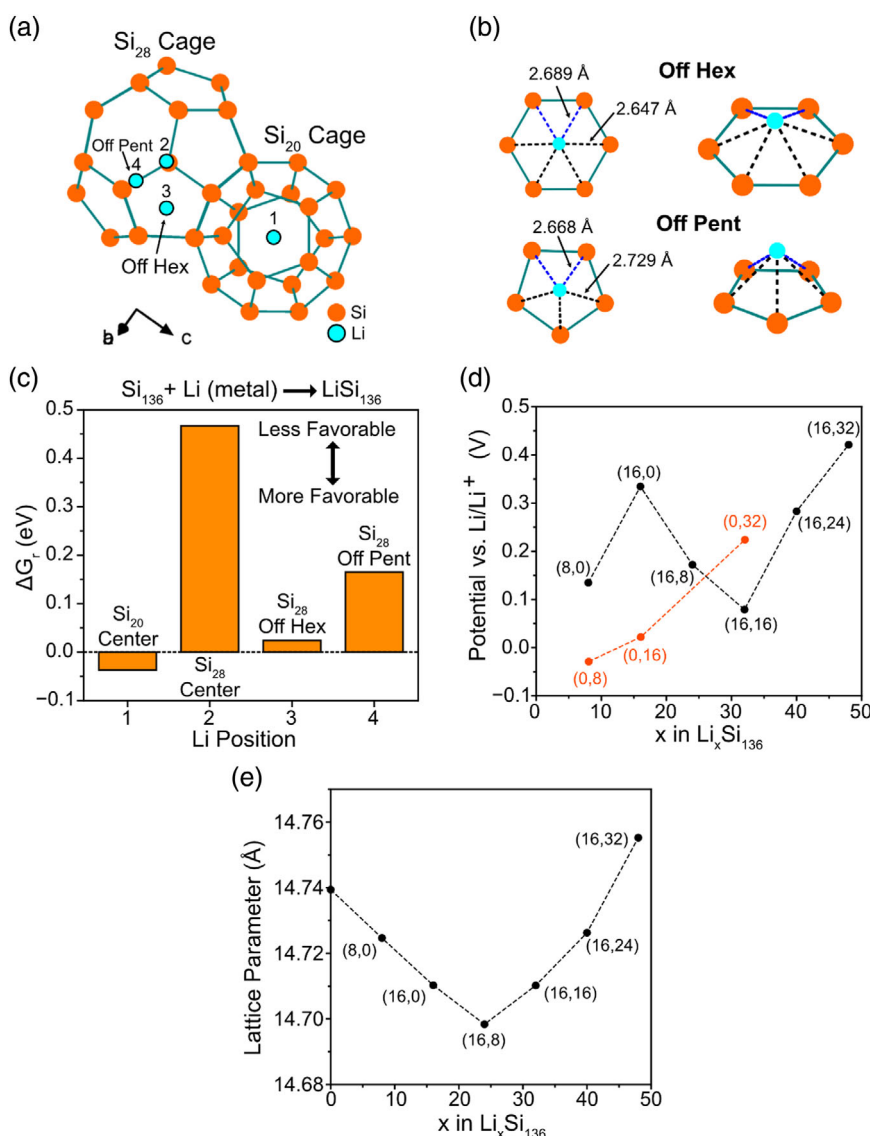


Figure 5. DFT calculations of Li positions in Si_{136} . a) Schematic of a Si_{28} cage connected with a Si_{20} cage showing the DFT calculated Li positions viewed down the [110] direction. b) Schematic of the "Off Hex" and "Off Pent" Li positions with select bond lengths. The blue colored bonds are provided to help visualize the change in orientation. c) Gibbs free energy of reaction (ΔG_r) for the reaction $\text{Si}_{136} + \text{Li (metal)} \rightarrow \text{LiSi}_{136}$ for each different Li position. d) Average lithiation voltage as a function of the Li content (x) in $\text{Li}_x\text{Si}_{136}$ where each point is identified by indices (a, b) where a = number of Li in the Si_{20} cage center (16c Wyckoff site) and b = number of Li in the "Off Hex" position within the Si_{28} cages (32e Wyckoff site). e) DFT calculated lattice constants for different amounts of Li in the Si_{136} lattice as shown in (d).

structure where Li only occupies each of the Si_{20} cage centers at (16, 0), the lattice parameter decreases when compared with empty, guest-free clathrate (from 14.74 to 14.71 Å). This result is similar to what has been reported for $\text{Na}_{24-x}\text{Si}_{136}$, where the Si_{136} framework contracts when Na occupies the Si_{28} cages, and is consistent with our previous calculations for $\text{Li}_{24}\text{Si}_{136}$.^[12,27] As Li is added to the "Off Hex" positions in the Si_{28} cages, the lattice parameter increases until reaching a value of 14.76 Å at a composition of $\text{Li}_{48}\text{Si}_{136}$, where all 32 possible "Off Hex" positions are filled. The PXRD results (Figure 4b) show an increase in the lattice parameter of around ≈ 0.01 Å after lithiation, whereas a decrease in the lattice parameter of ≈ 0.03 Å is

predicted by the calculation at the estimated composition of $x = 29\text{--}32$ Li. Therefore, both experimental and DFT results suggest that Li insertion into the Si_{136} lattice results in a very small volume change. More ab initio modeling and structural characterization, particularly in operando, will be needed to better elucidate the Li composition dependence on the clathrate lattice parameter.

From the combination of the electrochemical, structural, and computational results, we can, therefore, summarize the structure of Si_{136} after lithiation. **Figure 6** presents the guest-free, type-II Si clathrate structure before and after electrochemical lithiation, showing the proposed Li positions and estimated composition. The composition of $\text{Li}_{32}\text{Si}_{136}$ is primarily estimated

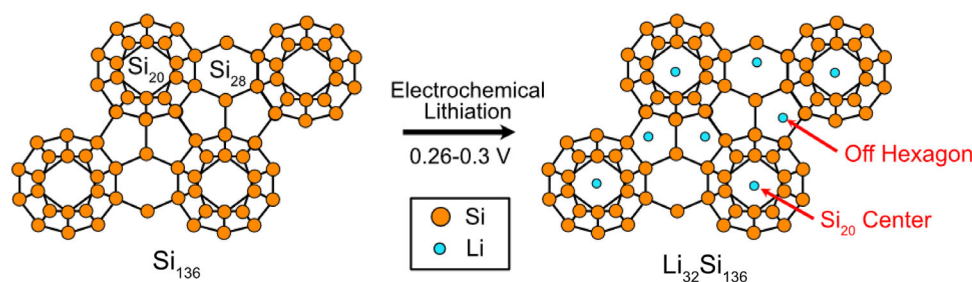


Figure 6. Schematic showing the lithium positions after electrochemical lithiation of Si_{136} . The Li atoms are proposed to occupy both Si_{20} and Si_{28} cages. In the Si_{28} cages, multiple Li reside in a single cage while occupying positions off of the hexagonal faces.

based on the electrochemical voltage profile (i.e., as shown in Figure 4a), as accurately assessing Li occupancy with PXRD is difficult especially when there is possible disorder on the sites. The identified Li positions, near the center of the Si_{20} cage and coordinated off the hexagonal faces in the Si_{28} cage, are supported by the PXRD refinement analysis (Figure 4) and match well with those predicted by DFT calculations (Figure 5). The preferred position of the Li guest atoms is cage-dependent. In the smaller Si_{20} cages composed solely of pentagonal faces, the Li atom prefers to be close to the cage center, with the PXRD analysis suggesting disorder on this position. In the larger Si_{28} cages comprised of pentagonal and hexagonal faces, the Li atom is predicted by DFT to be coordinated off the hexagonal faces of the cage ("Off Hex") due to the lower energy of this

position compared with the cage center or coordination off of a pentagonal face ("Off Pent").

2.5. Li Migration Pathways in Si_{136}

To identify the diffusion pathways for Li within the Si_{136} bulk structure, the climbing image NEB method^[39] was used. In our previous study, we investigated the migration barriers of Li in guest-free, type-I clathrate frameworks and found that Li migration between cages is mediated by the connection of hexagonal faces because of the lower migration barrier through these faces compared with the pentagonal ones.^[17] NEB calculations for Li migration between cages (i.e., intercage migration) in the guest-free, type-II Si clathrate structure are shown in Figure 7a.

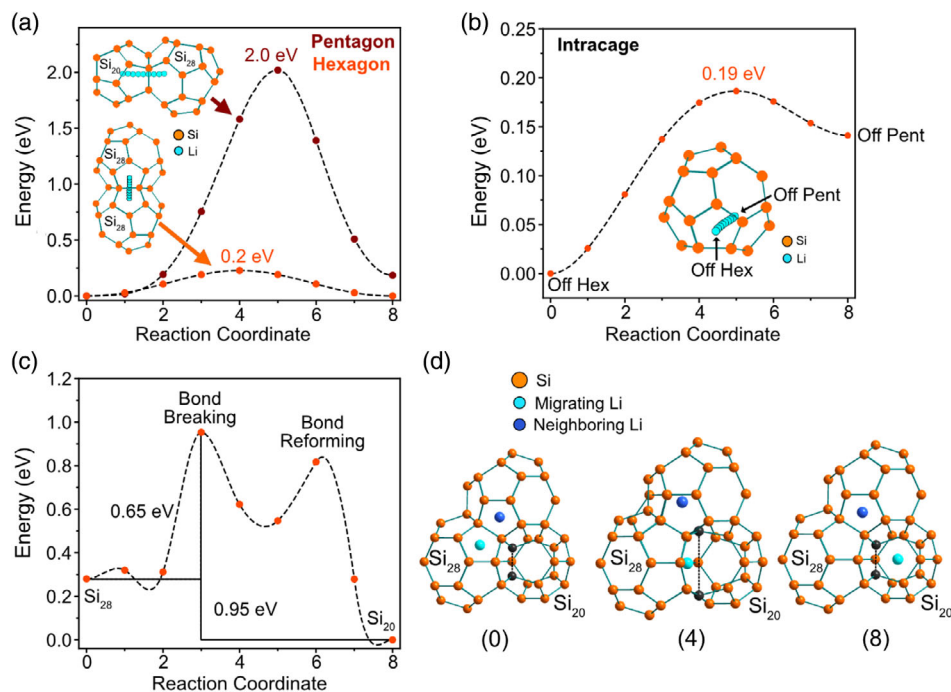


Figure 7. a) NEB-calculated minimum energy paths for migration of Li (cyan) in Si_{136} between the Si_{20} and Si_{28} cages through a shared pentagonal face (Pentagon path) and between the Si_{28} and Si_{28} cages through a shared hexagonal face (Hexagon path). b) NEB-calculated minimum energy path for Li between Off Hex and Off Pent positions in the Si_{28} cage; inset shows a schematic of the Si_{28} cage with the Li positions in the pathway. c) NEB-calculated minimum energy path for Li migrating from Si_{28} cage to the Si_{20} cage through a shared pentagonal face with a Li in the adjacent Si_{28} cage. d) Crystal model showing reaction coordinates 0, 4, and 8 of the NEB calculation in (c); the migrating Li is shown in cyan, the neighboring Li is in dark blue, and the Si atoms of the broken bond are in black.

Consistent with previous calculations, Li migration from the Si_{20} cage to the Si_{28} cage through a pentagonal face results in a higher energy barrier^[9,17] compared with Li migration between Si_{28} cages through a hexagonal face (2.0 vs 0.2 eV, respectively). Animations of these two migration paths can be found in Movies S2 and S3, Supporting Information. In both paths, the transition state involves the expansion of the pentagonal or hexagonal face as Li passes through the face center. The height of the barrier is correlated with the Li–Si distance at the transition state, and the degree to which the Si atoms bonded in the pentagonal/hexagonal face must move from their original positions to accommodate the migrating Li atom. As the hexagonal face has a larger cross-sectional area, acceptable Li–Si distances can be maintained with minimal disruption to the positions of the surrounding Si atoms as the Li passes through the hexagonal face, which results in a lower migration barrier. In contrast, the pentagonal transition state requires shorter Li–Si distances and a larger degree of movement of Si atoms, which results in a higher energy barrier for Li migration. Intracage migration (i.e., Li movement within the cage) was also considered for the Si_{28} cage due to the preference of Li to adopt an off-center position. The calculation showed a migration barrier of only 0.19 eV when Li moved from the “Off Hex” position to the “Off Pent” position (Figure 7b, and Movie S4, Supporting Information), meaning that Li would prefer to move along the side of the Si_{28} cage rather than through the center.

From these calculations, Li diffusion through the clathrate framework is predicted to be dominated by Li movement between the Si_{28} cages through the hexagonal faces, whereas diffusion into the Si_{20} cages from the Si_{28} cages is expected to be limited due to the high migration barrier of 2.0 eV (Pentagon path in Figure 7a). However, the PXRD refinement results (Figure 4b) provide support for Li occupation of the Si_{20} cages, meaning that there must be another possible pathway for Li insertion into the Si_{20} cages other than the aforementioned 2.0 eV pathway. As the Si_{20} cage is composed of only pentagonal faces, the low energy pathway through a hexagonal face (Hexagon path in Figure 7a) is not possible.

In our previous DFT study focused on guest-free, type-I clathrates, we found that Li could migrate into the Si_{20} cage of the type-I Si_{46} clathrate through a different pathway that involved temporary Si–Si bond breaking.^[17] If a Li atom was present in an adjacent cage, it could help to stabilize a transition state in which a Si–Si bond could lengthen to the extent that Li could migrate into the Si_{20} cage with a lower energy barrier than if it were to migrate through the center of the pentagonal face.^[17] To assess the feasibility of a similar mechanism in the type-II Si_{136} clathrate, the DFT calculation was repeated for Li migration from a Si_{28} to Si_{20} cage, but with the addition of a Li atom to an adjacent Si_{28} cage in the “Off Hex” position. The energy profile of this bond-breaking migration path is shown in Figure 7c, and the crystal schematic of the reaction coordinates 0, 4, and 8 is shown in Figure 7d (migrating Li atom shown in cyan). The reaction path starts with the migrating Li in the “Off Hex” position in the Si_{28} cage, and the ending position is the center of the Si_{20} cage. The results show that the lowest energy pathway for the migrating Li to enter the Si_{20} cage was not through the center of the pentagonal face, consistent with the high energy barrier of 2.0 eV, but rather “through” the bond connecting two of

the Si atoms in the pentagonal face (indicated by the black atoms in Figure 7d). This pathway, which effectively involves breaking and reformation of the Si–Si bond, has a migration barrier of only 0.65 eV, which is feasible for room temperature diffusion.^[40] Movies of these pathways with and without the neighboring Li atom can be found in Movies S5 and S6, Supporting Information. As Li moves through the center of the Si–Si bond, those Si atoms move away from the Li toward adjacent Si_{28} cages. It is interesting to note that the energetics of this migration process are asymmetric. When Li moves into the Si_{20} cage, the barrier is 0.65 eV, whereas it is 0.95 eV for the reverse process. This reflects the site preference for Li to be inside the Si_{20} cage, as shown in Figure 5d.

2.6. Reversible Li Insertion in Si_{136}

As the NEB calculations indicated the possibility of asymmetric energy barriers between Li insertion and deinsertion from the Si_{20} cages, the full lithiation and delithiation characteristics of the Na1 material were further investigated with electrochemical analysis. Previous studies conducted on guest-free Si_{136} only reported the lithiation characteristics;^[8] our previous study investigating both lithiation and delithiation was performed on Na-containing Si_{136} (i.e., $\text{Na}_{24}\text{Si}_{136}$) over a voltage range in which the clathrate structure transformed to amorphous phases.^[12] Therefore, the reversibility of the lithiation process within the potential window where the clathrate structure is intact has not been fully evaluated.

To investigate this, the Na1 electrode was cycled at 25 mA g^{−1} from 2.5 V to a voltage cutoff of 0.26 V versus Li/Li⁺ to allow lithium insertion only into the clathrate structure (i.e., preventing the Li alloying reaction below 0.25 V). The voltage profiles over the full potential range for the first three cycles are shown in Figure S4a, Supporting Information, whereas the zoomed-in region from 0.5 to 0.2 V is shown in Figure 8a for the first two cycles. A voltage cutoff of 0.26 V was chosen for cycles 1 and 2 to investigate only the Li insertion process (i.e., to prevent the amorphous phase transition). As evidenced by the very similar voltage profiles for the first two cycles, the Li insertion/deinsertion process into Si_{136} is presumed to take place in a reversible manner. The lower observed specific capacity in the second cycle is likely due to SEI formation. The different shapes of the lithiation versus delithiation curves, however, are an indication that these processes involve different Li reaction pathways. During lithiation, a voltage plateau (labeled as A) followed by a sloped region (B) is observed (Figure 8a). The voltage profile for delithiation is characterized by three distinct regions (labeled as C, D, and E), including a small peak (indicated by the asterisk), where the potential decreases and then increases again as Li is removed. This is unusual, as the potential typically only increases as the Li content is decreased. In the corresponding dQ/dE plot (Figure 8b), a broad peak centered at 0.32 V is observed during delithiation, corresponding to sloped voltage region C in Figure 8a, along with two sharper peaks at 0.34 and 0.36 V that correspond to the two quasi-plateaus in regions D and E, respectively.

To better understand these observations, the cutoff voltage for lithiation in the third cycle was increased to 0.29 V (Figure 8c), so that the process associated with sloped region B that was

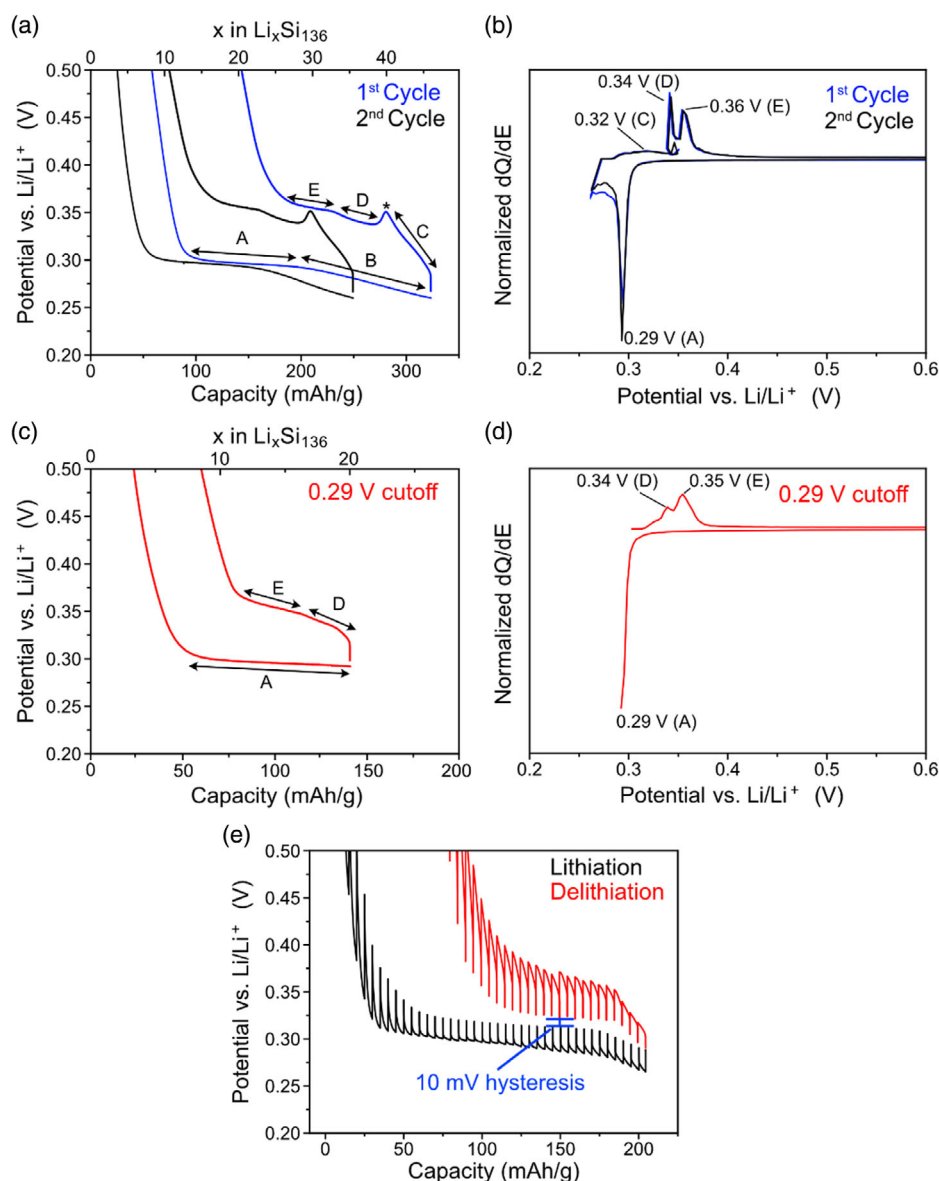


Figure 8. a) The lithiation and delithiation voltage profile of Na1 cycled with a lithiation cutoff voltage of 0.26 V at 25 mA g^{-1} (Cycle 1 and 2) with distinct voltage regions labeled with letters. b) Normalized dQ/dE derived from the voltage profiles with features corresponding to the regions in (a) labeled accordingly. c) The lithiation and delithiation voltage profile of Na1 cycled with a lithiation cutoff voltage of 0.29 V at 25 mA g^{-1} (Cycle 3) with distinct voltage regions labeled with letters. d) Normalized dQ/dE derived from the voltage profiles with features corresponding to the regions in (c) labeled accordingly. e) GITT profile of the lithiation and delithiation of Na1 at a current density of 10 mA g^{-1} with 30 min current pulses and 5 h relaxation time. The cell was cycled two times from 0.27 to 2.5 V prior to the GITT experiment. Zoomed-out versions of these plots can be found in Figure S4, Supporting Information.

observed in the first two cycles was prevented. Notably, sloped region C and corresponding peak in the dQ/dE plot (Figure 8d) were absent in the subsequent delithiation profile. This suggests that the processes associated with region C during delithiation correspond to the reverse of reaction B in the lithiation profile. Overall, these results provide strong support that the observed plateau at 0.30 V (region A) corresponds to a reversible reaction with a reproducible, albeit, asymmetric voltage profile with two distinct regions of Li insertion.

To obtain a better understanding of the energetics of the lithiation and delithiation pathways, the galvanostatic intermittent titration technique (GITT)^[41] was used to observe the polarization of the lithiation and delithiation reactions in Na1 (Figure 8e, an expanded view is shown in Figure S4b, Supporting Information; here, polarization refers to the difference in potential in the cell during galvanostatic vs open circuit conditions). Most notably, the voltage hysteresis after relaxation between lithiation and delithiation is around 10 mV, which is

similar to the hysteresis seen in traditional insertion electrode materials (i.e., LiFePO_4 , LiCoO_2).^[42] The low voltage hysteresis is strong support of a topotactic insertion reaction, as it shows that the electrode is in a similar structural state after the current pulses during both lithiation and delithiation. Another notable point is that the polarization is higher during delithiation (40–60 mV) than lithiation (20 mV). We speculate that this could indicate different kinetics for lithiation and delithiation, which could be related to the origin of the asymmetric voltage profile and is also supported by the asymmetric migration barriers observed in the NEB calculations (Figure 7c).

The GITT profile also shows an irreversible capacity loss of 22% between the lithiation and delithiation charge capacities. Note that two galvanostatic cycles (without rest periods) were performed prior to the GITT measurement to ensure the formation of the SEI, and in general, the clathrate shows high coulombic efficiencies after the first cycle loss (>95%). The origin of this behavior is currently unknown but could be related to larger amounts of SEI formation, as the electrode spends much longer times at the low potentials than in a regular cycling experiment (see GITT profile in terms of time, Figure S4c,d, Supporting Information). It has been previously shown that the SEI growth on Si clathrates can be problematic depending on the processing conditions of the clathrate.^[13,18] Another potential explanation for the irreversible capacity is the trapping of Li during relaxation, which could be related to the higher polarizations found during delithiation. The hypothesis is supported by the observation that the GITT voltage profile (Figure 8e) does not show the peak labeled with the asterisk seen in the galvanostatic

curve (Figure 8a), suggesting that the periods of relaxation have an effect on the delithiation pathway.

Next, galvanostatic cycling experiments were conducted to evaluate the long-term cycling stability of the NaI clathrate with two voltage cutoffs for lithiation (the delithiation cutoff voltage was fixed at 2.5 V). For the cell with 0.26 V cutoff (Figure 9a), the initial capacity was 275 mAh g^{-1} (the first cycle efficiency of 68%), which decreased to 200 mAh g^{-1} in the second cycle. The capacity then increased to 225 mAh g^{-1} over ten cycles and then began to decrease to 100 mAh g^{-1} after 50 cycles. The coulombic efficiency reached >98.5% past cycle 10 and continued to increase during cycling (Figure 9b). For the cell with 0.28 V cutoff, the cycling stabilized around 90 mAh g^{-1} and reached 60 mAh g^{-1} after 50 cycles. The analysis of the voltage profiles for the cell with 0.26 V cutoff (Figure 9c) showed that the shape of the delithiation curves changed with cycling. At cycles 10 and 20, the plateau attributed to clathrate delithiation at 0.34–0.36 V decreased in favor of a sloped feature around 0.5–0.6 V. This sloped feature is similar to the voltage reported for the delithiation of amorphous Si.^[31,32] We speculate that when the lithiation voltage cutoff is too low, some of the clathrate could be converted to an amorphous Li_xSi phase through an alloying reaction, as evidenced by its different delithiation voltage profile indicated in Figure 9c. Analysis of the cell with 0.28 V cutoff (Figure 9d) shows that the shape of the voltage curve is retained during cycling, suggesting that using the higher voltage cutoff circumvented the suspected amorphization reaction. On this basis, we suspect that the better capacity retention obtained when using the 0.28 V cutoff is due to mitigation of the

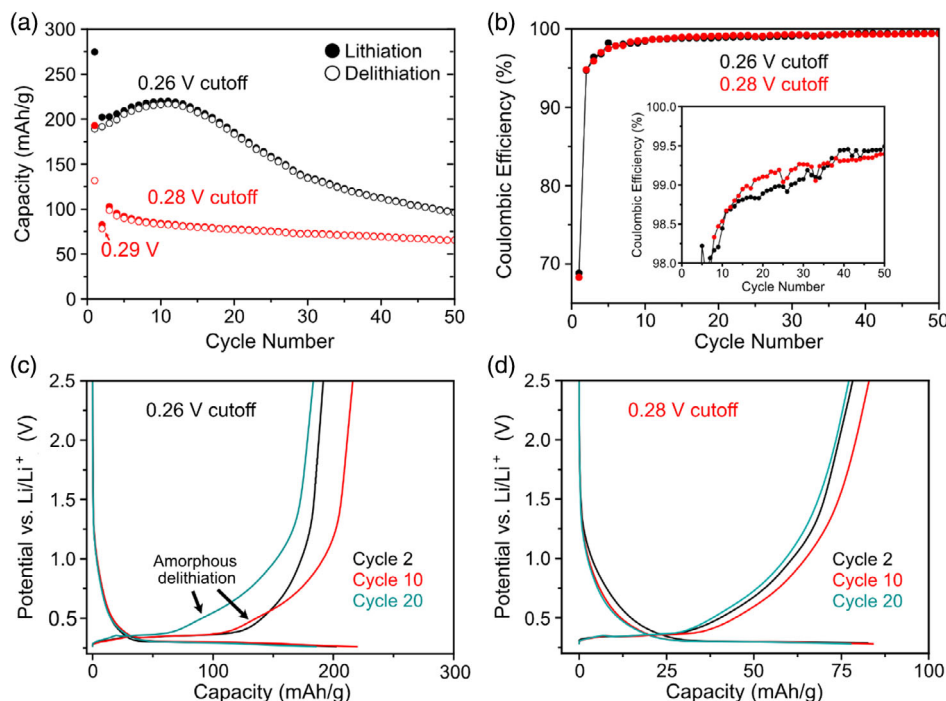


Figure 9. a) Voltage profile of NaI cycled at 25 mA g^{-1} with a voltage cutoff of 0.26 and 0.28 V. b) Coulombic efficiency versus cycle number. c) Voltage profiles of the 2nd, 10th, and 20th cycle with a 0.26 V voltage cutoff showing the increase of amorphous reactions at longer cycles. d) Voltage profile of NaI cycled at 25 mA g^{-1} with a voltage cutoff of 0.28 V.

amorphous phase transformation (i.e., preventing transformation of crystalline $\text{Li}_x\text{Si}_{136}$ to amorphous Li_xSi). PXRD of the electrodes after 50 cycles (Figure S5, Supporting Information) showed that reflections from the type-II Si clathrate were still present when using both voltage cutoffs, suggesting that the majority of the crystalline clathrate phase structure was retained despite the suspected amorphous phase formation in some of the sample, and further supporting a topotactic mechanism.

2.7. Structural Origins of Li Insertion in Clathrate Materials

For topotactic Li insertion to occur, there must be facile migration between Li sites in the host crystal. Based on the observed and calculated Li positions from the PXRD and DFT analysis, the possible Li diffusion pathways in the cage structure can be postulated. First, we point out the importance having a low enough Na content in the cages to observe the Li insertion plateau at 0.30 V. This is demonstrated in Figure 3, where this feature is absent from the $\text{Na}_{10.7}\text{Si}_{136}$ (Na11) electrode. Because the Na guest atoms preferentially occupy the large Si_{28} cages in $\text{Na}_{24-x}\text{Si}_{136}$, this means that in $\text{Na}_{10.7}\text{Si}_{136}$, the eight Si_{28} cages are occupied by Na atoms, whereas most of the 16 Si_{20} cages are unoccupied. The fact that this Li insertion plateau at 0.30 V is not observed when the Si_{28} cages are occupied by Na implies that the presence of unoccupied Si_{28} cages is an important condition for the reversible Li insertion process to occur.

Considering the NEB calculations presented in Figure 7a, it is evident that Li diffusion into the Si_{28} cages compared with the Si_{20} cages is favored due to the lower energy barrier for the hexagonal transition state (0.2 eV). As the Si_{28} cages form a tetrahedral network of hexagonal face sharing cages (Figure 1b), the lowest energy pathway for Li to migrate through the bulk structure would be through this Si_{28} cage network. On the basis of the high migration barrier for Li diffusion through the pentagonal face (2.0 eV), one would expect that Li could not occupy the Si_{20} cages (composed of only pentagonal faces), because the barrier to enter the cage is too high for room temperature migration. However, the PXRD results (Figure 4b) show significant Li occupation in the Si_{20} cages, meaning that a different pathway must be taken for Li to enter the Si_{20} cages. As described previously, a pathway involving temporary bond breaking allows Li to enter the Si_{20} cage with a much lower migration barrier of 0.65 eV. This bond-breaking migration path has been calculated

previously in several other situations, such as Li migration in $\text{LiBa}_8\text{Si}_{136}$ and $\text{Li}_6\text{Si}_{46}$ and for Na migration in the Si_{20} cages of Si_{46} and Si_{136} .^[9,17] In the case of Li, the pathway is energetically feasible if there is another guest atom in the cage adjacent to the transition state. Yang and Tse posited that the extra electron density from the neighboring guest atom could aid in stabilizing the transition state, thus allowing access to the bond-breaking pathway.^[9] We agree with this hypothesis and speculate that a cooperative migration mechanism involving multiple Li could be important for Li to access the Si_{20} cages of the clathrates by bypassing the pentagonal transition state.

Another notable aspect of the bond-breaking migration pathway is the observed energetic asymmetry when Li migrates between the Si_{28} and Si_{20} cages. Migration from the Si_{28} cage to the Si_{20} has a barrier of 0.65 eV, whereas moving in the reverse pathway would have a barrier of 0.95 eV (Figure 7c). If we assume that the prominent pathway for Li to occupy a Si_{20} cage is by migration from a Si_{28} cage (as opposed to migration from Si_{20} to Si_{20}), it is expected that there will be an asymmetry in the migration barrier due to the difference in site energies within Si_{20} and Si_{28} cages, which is shown in Figure 5d. We speculate that this asymmetry could be related to the asymmetry seen in the delithiation voltage profile (Figure 8a,b) and the GITT polarization (Figure 8e). According to the DFT calculations, Li occupation of the Si_{20} cages is most energetically favorable (Figure 5c), which means that these sites should be filled first upon lithiation. However, for Li to enter the Si_{20} cage is expected to be kinetically difficult and requires a cooperative Li migration path with Li in the Si_{28} cages. If the Si_{28} cages were not the main Li pathway, then it is expected that the Na11 electrode (where Si_{28} cages are filled by Na) would display electrochemical voltage characteristics similar to those in Na1. As this is not the case (Figure 3), we can presume that Li first travels through the Si_{28} cages and then migrates into the Si_{20} cages.

On the basis of the structural, electrochemical, and DFT analyses described earlier, we therefore summarize the Li migration pathway through the Si_{136} type-II clathrate structure as shown in Figure 10, with the red arrow showing the continuous Li migration pathway through the Si_{28} cages connected via hexagonal faces (atoms in the hexagon shown in yellow). Along the migration “highway,” Li can migrate into the Si_{20} cages, possibly via the bond-breaking pathway shown in Figure 7d. During delithiation, Li will also need to leave via the Si_{28} “Li highway,” but the barrier

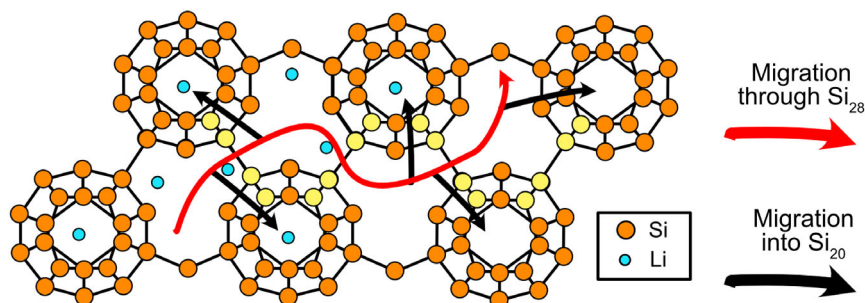


Figure 10. Schematic showing the proposed Li pathways through the type-II Si_{136} clathrate structure. Li migration would primarily occur through the interconnected Si_{28} cages via the hexagonal transition states (Si atoms in the hexagons are shown in yellow) due to the low energy barrier of 0.2 eV. For the Li to access the Si_{20} cages, it must first travel to an adjacent Si_{28} cage and then enter the Si_{20} cage via the bond-breaking mechanism shown in Figure 7d.

to go back into the Si₂₈ cage is predicted to be higher via the bond-breaking mechanism because of the higher site energy of the Si₂₈ cage. We speculate that the unusual delithiation voltage profile could be related to this need for Li to travel through the Si₂₈ cages for bulk diffusion, which results in different Li structuring than during lithiation. More detailed ab initio modeling and in situ characterization would be required for elucidating the exact mechanism.

From our analysis, we conclude that topotactic Li insertion into guest free, type-II Si clathrates is feasible due to the fulfillment of two important requirements: 1) stable Li positions in the structure, and 2) facile Li diffusion into the host structure. If considering α -Si with the diamond cubic structure, Li insertion into the tetrahedral position is energetically unfavorable due to expansion of the surrounding Si atoms,^[43] but Li diffusion between these positions shows a reasonable calculated migration barrier of 0.62 eV.^[43,44] In contrast, the larger cavities of the guest-free, type-II Si clathrate allow the Li to be inserted without perturbing the Si framework, resulting in more favorable lithiation energetics. Another important factor is that the distance between adjacent Li positions is larger in the clathrate structure than in α -Si. As described by Zhao et al., as Li enters adjacent tetrahedral positions in α -Si, it becomes more favorable for Li to surround and then break a Si–Si bond, which could lead to the beginning of amorphization.^[45] Based on the low energy migration pathways in Si₁₃₆ and the larger distance between adjacent Li positions (4.85–5.43 Å), we hypothesize that the amorphization reaction is kinetically bypassed, because Li atoms are able to spread throughout the lattice and fill the vacant cages without surrounding the Si–Si bonds. Only after the open framework is filled with Li does it become feasible for the conversion reaction to begin and form amorphous Li_xSi. The analysis presented here demonstrates how the cage structure of Si clathrates results in novel electrochemical properties originating primarily from low energy barrier Li migration throughout the bulk structure.

Now that the structural framework for enabling Li insertion has been established, and we can consider other Tetrel clathrate-like materials within this framework. In our previous DFT study focused on type-I clathrates, we concluded that Li diffusion would be preferred within the 1D channels of Si₂₄ cages connected by hexagonal faces.^[17] Based on the results reported here for the type-II clathrates, we expect to see similar insertion behavior in Si₄₆ as in Si₁₃₆, although this is difficult to experimentally verify due to the synthetic challenges of obtaining guest-free Si₄₆ of high purities and quantities. Notably, Si₄₆ with the type-I clathrate structure has a higher ratio of hexagon containing polyhedra to Si₂₀ polyhedra (6:2), suggesting that the hypothesized bond-breaking pathway for Li to enter the Si₂₀ cage may play less of a role on the insertion properties. A recently discovered Si clathrate-like polymorph, Si₂₄,^[46] was reported with low calculated Li migration barriers (0.1 eV) through 1D hexagon-like channels^[47] and is expected to demonstrate Li insertion characteristics based on the results here. Guest-free, type-II Ge (Ge₁₃₆)^[20] has previously been investigated for battery applications, and a continuous increase in the lattice parameter was observed with increased lithiation,^[11] thus implying the occupation of Li within the framework. As Ge₁₃₆ shares the same structure as Si₁₃₆, we expect to see Li insertion behavior

but with more off-center Li positions and lower migration barriers due to the larger Ge cage sizes.

For all of these materials, it is also important to consider the possibility of alloying/conversion reactions that occur in a similar voltage range to Li insertion. The competition between insertion and conversion reactions is determined by a close interplay between kinetics and thermodynamics. As described by Hannah et al., insertion is expected to occur prior to a conversion reaction if the voltage for Li insertion is higher than the voltage for conversion and if the kinetics are favorable for insertion.^[48] Thus, it is important for the Li site energy in the Tetrel framework to be stable enough (at high enough voltage vs Li/Li⁺) and accompanied by facile diffusion to be competitive with possible alloying reactions. In the case of Si₁₃₆, Li insertion is observed at 0.30 V, whereas the alloying reaction occurs at 0.25 V, confirming that this requirement is satisfied for the type-II Si clathrate. However, based on the higher voltage of the alloying reaction for Si₁₃₆ (0.25 V) compared with that in α -Si and Na_{10.7}Si₁₃₆ (0.10–0.15 V), we suspect that Li insertion through the bulk clathrate enables an alternative alloying pathway that is more similar to what occurs in lithiation of amorphous Si. Future work will be dedicated toward understanding the structural differences between alloying reactions in the type-II Si clathrate and other Si structures to understand the amorphous phase formation mechanisms.

2.8. Implications for Li-ion Battery Anodes

Given the Li insertion characteristics for the type-II Si clathrate discussed earlier, we now discuss the potential implications for using these materials as Li-ion battery anodes. If a capacity of 231 mAh g^{−1} (468 Ah L^{−1}) is assumed based on the composition of Li₃₂Si₁₃₆ that forms at a reaction of voltage of 0.30 V versus Li/Li⁺, then the electrochemical properties are competitive with other insertion anode materials. For instance, spinel Li₄Ti₅O₁₂ (LTO) has a capacity of 175 mAh g^{−1} (500 Ah L^{−1})^[49] at 1.55 V versus Li/Li⁺, meaning that the clathrate would have a higher energy density due to the comparable capacity but lower reaction voltage of 0.30 V, which would result in a larger cell voltage when partnered with a cathode in a full cell. Another notable feature of Li insertion into Si₁₃₆ is the very small volume expansion of $\approx 0.2\%$, meaning that the insertion process could be considered “zero strain,” similar to LTO. In addition, the voltage profile between lithiation and delithiation displays low hysteresis, which is advantageous for high energy efficiency. Although only a composition of Li₃₂Si₁₃₆ was achieved experimentally, DFT calculations suggested that Li₄₈Si₁₃₆ would be energetically favorable with a low predicted volume expansion of 0.31% (Figure 5d,e). If this structure (Li₄₈Si₁₃₆) could be achieved, it would have a capacity of 346 mAh/g (703 Ah/L), which would be comparable to graphite (372 mAh g^{−1}, 719 Ah L^{−1}) but with much lower predicted volume expansion (0.31% vs 13% for graphite^[50]). Based on these reasons, guest-free, type-II Si clathrates could be very promising Li-ion insertion anodes, and further research into their electrochemical properties is warranted.

For practical applications, there are several obstacles that still need to be overcome. Most notably, the voltage range for the Li

insertion process (0.26–0.30 V vs Li/Li⁺) is close to the potential at which the conversion reaction to the Li_xSi amorphous phase takes place (0.25 V), and therefore, the cutoff voltage must be carefully controlled. From our cycling experiments, we found that if the voltage cutoff was too close to the potential at which the conversion reaction initiated, the amorphous phase transition could partially take place and result in poorer capacity retention. The irreversible capacity loss due to SEI formation, particularly in the first cycle, also needs to be addressed, possibly through previously established methods used for other anode materials, such as electrode pre-treatment or electrolyte additives.^[51] More studies will be needed to investigate the long-term cycling behavior and stability of Si clathrates as a host for Li.

3. Conclusion

In this work, the structural origins of the electrochemical properties of type-II Si clathrate were investigated with synchrotron X-ray characterization and DFT calculations. Type-II Si clathrate samples with compositions of Na_{0.9(1)}Si₁₃₆ (Na1) and Na_{10.7(1)}Si₁₃₆ (Na11) were synthesized, and synchrotron PXRD patterns were refined to determine the starting Na content and structure after lithium insertion. The lithiation of Na1 and Na11 is accompanied by distinctly different voltage profiles, demonstrating the importance of the Na content on their electrochemical properties. In the nearly guest-free Na1 clathrate, topotactic Li insertion is observed, which is a unique characteristic, because Tetrel elemental compounds typically undergo Li alloying reactions. The voltage plateau at 0.30 V versus Li/Li⁺ is attributed to Li insertion into both Si₂₀ and Si₂₈ cages, likely with multiple guest atoms within the larger Si₂₈ cages, as supported by Rietveld refinement of synchrotron PXRD measurements and DFT calculations. Na11 does not show the same insertion behavior, suggesting that vacant Si₂₈ cages are key to enabling Li insertion reactions rather than conversion reactions that form amorphous phases. For the first time, we demonstrate the reversible cycling of Li in the type-II Si clathrate, which shows a reproducible voltage profile that is asymmetric but features low hysteresis. NEB calculations show that Li migration barriers between interconnected Si₂₈ cages are low (0.2 eV) through the center of the hexagonal face. In contrast, Li migration through the center of a pentagonal face for movement between Si₂₀ and Si₂₈ cages has a high energy barrier of 2.0 eV unless Li is present in an adjacent Si₂₈ cage, which can facilitate a lower energy pathway (0.65 eV) that involves temporary Si–Si bond breaking. The latter pathway may be responsible for the asymmetry observed in the voltage profile. In summary, we attribute the structural origin of Li insertion in Si₁₃₆ to the energetically favorable Li insertion sites in the Si clathrate cages and facile diffusion paths throughout the bulk structure. Importantly, we identify the migration pathway through Si hexagonal faces as an important condition for enabling bulk Li diffusion. On the basis of this structural feature, we speculate that other open Tetrel frameworks such as Si₄₆, Si₂₄, and Ge₁₃₆ could also demonstrate reversible Li insertion with low volume expansion, which could be promising for possible applications as Li-ion battery anodes.

4. Experimental and Computational Methods

The Na_{0.9}Si₁₃₆ (Na1) and Na_{10.7}Si₁₃₆ (Na11) clathrates were synthesized by thermal decomposition of Na₄Si₄ under vacuum using methods modified from previous reports.^[19,52] The clathrates were prepared into electrodes on Cu foil with carbon black as a conducting additive and polyvinylidene difluoride (PVDF) as a binder. The electrodes were lithiated galvanostatically in half-cells with lithium metal and then extracted for ex situ PXRD measurements. Cycling experiments were conducted in CR2032 coin cells using lithium metal as the counter electrode. Synchrotron XRD measurements were performed at the 11-BM beamline at the Advanced Photon Source (APS) at the Argonne National Laboratory ($\lambda = 0.41284$ Å for analysis of as-synthesized samples and $\lambda = 0.412781$ Å for analysis of samples after lithiation) and the P02.1 powder diffraction beamline ($\lambda = 0.20733$ Å) at PETRA III at the Deutsches Elektronen-Synchrotron (DESY). The first-principles DFT calculations were performed in a similar manner to our previous work^[14,16,17] and are described in more detail in the Supporting Information. The Gibbs free energy change and average lithiation voltages were calculated as described previously.^[14] The climbing image NEB method was used to calculate the Li migration barriers.^[39] More detailed descriptions of the synthesis, electrochemical and synchrotron measurements, and refinements are in the Supporting Information.

Supporting Information

Supporting Information is available from the Wiley Online Library or from the author.

Acknowledgements

This work was supported by funding from National Science Foundation, Division of Materials Research awards 1710017, 1709813, 2004514, and 2004579. A.D. and J.M.W. acknowledge support from ASU Fulton Schools of Engineering Dean's Fellowships. C.K.C. acknowledges support from the Max Planck Society as well as the Alexander von Humboldt Foundation for a Humboldt Research Fellowship. The authors acknowledge the use of facilities within the Eyring Materials Center at Arizona State University supported in part by NNCI-ECCS-1542160 and the use of the Research Computing at Arizona State University for providing high-performance computing resources that have contributed to the research results reported within this article. The authors also acknowledge the use of the services from the Instrumental Design and Fabrication Core Facility at Arizona State University. The authors also thank Deutsches Elektronen-Synchrotron (Hamburg, Germany) for access to beamline P02.1 (proposal no. I-20180707) and J. Tseng for assistance with synchrotron XRD measurements. The use of the APS at Argonne National Laboratory through the 11-BM mail in program (Proposal-63359, 66690) was supported by the U.S. Department of Energy, Office of Science, Office of Basic Energy Sciences, under Contract No. DE-AC02-06CH11357.

Conflict of Interest

The authors declare no conflict of interest.

Data Availability Statement

Research data are not shared.

Keywords

anodes, clathrate, insertion, Li-ion batteries

Received: December 31, 2020

Revised: February 4, 2021

Published online: March 8, 2021

- [1] J. Dolyniuk, B. Owens-baird, J. Wang, J. V. Zaikina, K. Kovnir, *Mater. Sci. Eng. R* **2016**, 108, 1.
- [2] A. D. Martinez, L. Krishna, L. L. Baranowski, M. T. Lusk, E. S. Toberer, A. C. Tamboli, *IEEE J. Photovoltaics* **2013**, 3, 1305.
- [3] T. Kume, F. Ohashi, K. Sakai, A. Fukuyama, M. Imai, H. Udono, T. Ban, H. Habuchi, H. Suzuki, T. Ikari, S. Sasaki, S. Nonomura, *Thin Solid Films* **2016**, 609, 30.
- [4] T. Fix, R. Vollondat, A. Ameer, S. Roques, J. L. Rehspringer, C. Chevalier, D. Muller, A. Slaoui, *J. Phys. Chem. C* **2020**, 124, 14972.
- [5] J. M. Hübner, Y. Prots, W. Schnelle, M. Bobnar, M. König, M. Baitinger, P. Simon, W. Carrillo-Cabrera, A. Ormeci, E. Svanidze, Y. Grin, U. Schwarz, *Chem. – A Eur. J.* **2020**, 26, 830.
- [6] D. Connétable, V. Timoshevskii, B. Masenelli, J. Beille, J. Marcus, B. Barbara, A. M. Saitta, G. M. Rignanese, P. Mélinon, S. Yamanaka, X. Blase, *Phys. Rev. Lett.* **2003**, 91, 247001.
- [7] S. Yamanaka, E. Enishi, H. Fukuoka, M. Yasukawa, *Inorg. Chem.* **2000**, 39, 56.
- [8] T. Langer, S. Dupke, H. Trill, S. Passerini, H. Eckert, R. Pöttgen, M. Winter, *J. Electrochem. Soc.* **2012**, 159, A1318.
- [9] J. Yang, J. S. Tse, *J. Mater. Chem. A* **2013**, 1, 7782.
- [10] A. Dopilka, A. Childs, S. Bobev, C. K. Chan, *Chem. Mater.* **2020**, 32, 9444.
- [11] B. Böhme, C. B. Minella, F. Thoss, I. Lindemann, M. Rosenburg, C. Pistidda, K. T. Möller, T. R. Jensen, L. Giebel, M. Baitinger, O. Gutfleisch, H. Ehrenberg, J. Eckert, Y. Grin, L. Schultz, *Adv. Eng. Mater.* **2014**, 16, 1189.
- [12] N. A. Wagner, R. Raghavan, R. Zhao, Q. Wei, X. Peng, C. K. Chan, *ChemElectroChem* **2014**, 1, 347.
- [13] Y. Li, R. Raghavan, N. A. Wagner, S. K. Davidowski, L. Baggetto, R. Zhao, Q. Cheng, J. L. Yarger, G. M. Veith, C. Ellis-Terrell, M. A. Miller, K. S. Chan, C. K. Chan, *Adv. Sci.* **2015**, 2, 1500057.
- [14] X. Peng, Q. Wei, Y. Li, C. K. Chan, *J. Phys. Chem. C* **2015**, 119, 28247.
- [15] R. Zhao, S. Bobev, L. Krishna, T. Yang, J. M. Weller, H. Jing, C. K. Chan, *ACS Appl. Mater. Interfaces* **2017**, 9, 41246.
- [16] A. Dopilka, R. Zhao, J. M. Weller, S. Bobev, X. Peng, C. K. Chan, *ACS Appl. Mater. Interfaces* **2018**, 10, 37981.
- [17] A. Dopilka, X. Peng, C. K. Chan, *J. Phys. Chem. C* **2019**, 123, 22812.
- [18] T. Tarnev, P. Wilde, A. Dopilka, W. Schuhmann, C. K. Chan, E. Ventosa, *ChemElectroChem* **2020**, 7, 665.
- [19] J. S. Kasper, P. Hagenmuller, M. Pouchard, C. Cros, *Science* **1965**, 150, 1713.
- [20] A. M. Guloy, R. Ramlau, Z. Tang, W. Schnelle, M. Baitinger, Y. Grin, *Nature* **2006**, 443, 320.
- [21] L. L. Baranowski, L. Krishna, A. D. Martinez, T. Raharjo, V. Stevanović, A. C. Tamboli, E. S. Toberer, *J. Mater. Chem. C* **2014**, 2, 3231.
- [22] B. Böhme, K. Wei, M. Bobnar, Y. Prots, U. Burkhardt, M. Baitinger, G. S. Nolas, Y. Grin, *Zeitschrift für Krist. – Cryst. Mater.* **2017**, 232, 543.
- [23] M. C. Schäfer, S. Bobev, *J. Am. Chem. Soc.* **2013**, 135, 1696.
- [24] M. C. Schäfer, S. Bobev, *Inorganics* **2014**, 2, 79.
- [25] E. Reny, P. Gravereau, C. Cros, M. Pouchard, *J. Mater. Chem.* **1998**, 8, 2839.
- [26] G. K. Ramachandran, J. Dong, J. Diefenbacher, J. Gryko, R. F. Marzke, O. F. Sankey, P. F. McMillan, *J. Solid State Chem.* **1999**, 145, 716.
- [27] M. Beekman, E. N. Nenghabi, K. Biswas, C. W. Myles, M. Baitinger, Y. Grin, G. S. Nolas, *Inorg. Chem.* **2010**, 49, 5338.
- [28] S. Stefanoski, C. D. Malliakas, M. G. Kanatzidis, G. S. Nolas, *Inorg. Chem.* **2012**, 51, 8686.
- [29] B. Key, R. Bhattacharyya, M. Morcrette, V. Seznéc, J. M. Tarascon, C. P. Grey, *J. Am. Chem. Soc.* **2009**, 131, 9239.
- [30] B. Key, M. Morcrette, J.-M. Tarascon, C. P. Grey, *J. Am. Chem. Soc.* **2011**, 133, 503.
- [31] M. N. Obrovac, L. Christensen, *Electrochem. Solid-State Lett.* **2004**, 7, A93.
- [32] M. J. Loveridge, M. J. Lain, I. D. Johnson, A. Roberts, S. D. Beattie, R. Dashwood, J. A. Darr, R. Bhagat, *Sci. Rep.* **2016**, 6, 1.
- [33] M. N. Obrovac, L. J. Krause, *J. Electrochem. Soc.* **2007**, 154, A103.
- [34] S. Yamanaka, M. Komatsu, M. Tanaka, H. Sawa, K. Inumaru, *J. Am. Chem. Soc.* **2014**, 136, 7717.
- [35] J. He, D. D. Klug, K. Uehara, K. F. Preston, C. I. Ratcliffe, J. S. Tse, *J. Phys. Chem. B* **2001**, 105, 3475.
- [36] M. Aydinol, A. Kohan, G. Ceder, K. Cho, J. Joannopoulos, *Phys. Rev. B – Condens. Matter Mater. Phys.* **1997**, 56, 1354.
- [37] A. Van Der Ven, Z. Deng, S. Banerjee, S. P. Ong, *Chem. Rev.* **2020**, 120, 6977.
- [38] U. Arrieta, N. A. Katcho, O. Arcelus, J. Carrasco, *Sci. Rep.* **2017**, 7, 5350.
- [39] G. Henkelman, B. P. Uberuaga, H. Jónsson, *J. Chem. Phys.* **2000**, 113, 9901.
- [40] Z. Rong, R. Malik, P. Canepa, G. Sai Gautam, M. Liu, A. Jain, K. Persson, G. Ceder, *Chem. Mater.* **2015**, 27, 6016.
- [41] W. Weppner, R. A. Huggins, *J. Electrochem. Soc.* **1977**, 124, 1569.
- [42] W. Dreyer, J. Jamnik, C. Gohlke, R. Huth, J. Moškon, M. Gaberšček, *Nat. Mater.* **2010**, 9, 448.
- [43] C. Y. Chou, H. Kim, G. S. Hwang, *J. Phys. Chem. C* **2011**, 115, 20018.
- [44] H. Kim, K. E. Kweon, C. Y. Chou, J. G. Ekerdt, G. S. Hwang, *J. Phys. Chem. C* **2010**, 114, 17954.
- [45] K. Zhao, W. L. Wang, J. Gregoire, M. Pharr, Z. Suo, J. J. Vlassak, E. Kaxiras, *Nano Lett.* **2011**, 11, 2962.
- [46] D. Y. Kim, S. Stefanoski, O. O. Kurakevych, T. A. Strobel, *Nat. Mater.* **2015**, 14, 169.
- [47] Y. He, X. Lu, D. Y. Kim, *RSC Adv.* **2018**, 8, 20228.
- [48] D. C. Hannah, G. Sai Gautam, P. Canepa, G. Ceder, *Adv. Energy Mater.* **2018**, 1800379, 1.
- [49] T. Ohzuku, A. Ueda, N. Yamamoto, *J. Electrochem. Soc.* **1995**, 142, 1431.
- [50] S. Schweidler, L. De Biasi, A. Schiele, P. Hartmann, T. Brezesinski, J. Janek, *J. Phys. Chem. C* **2018**, 122, 8829.
- [51] V. Aravindan, Y. S. Lee, S. Madhavi, *Adv. Energy Mater.* **2017**, 7, 1.
- [52] L. Krishna, L. L. Baranowski, A. D. Martinez, C. A. Koh, P. C. Taylor, A. C. Tamboli, E. S. Toberer, *CrystEngComm* **2014**, 16, 3940.